

## Flow-through electroporation of mammalian cells in decoupled flow streams using microcapillaries

Yuan Luo and Levent Yobas

Citation: *Biomicrofluidics* **8**, 052101 (2014); doi: 10.1063/1.4879155

View online: <http://dx.doi.org/10.1063/1.4879155>

View Table of Contents: <http://scitation.aip.org/content/aip/journal/bmf/8/5?ver=pdfcov>

Published by the [AIP Publishing](#)

---

### Articles you may be interested in

[Individually addressable multi-chamber electroporation platform with dielectrophoresis and alternating-current-electro-osmosis assisted cell positioning](#)

*Biomicrofluidics* **8**, 024117 (2014); 10.1063/1.4873439

[Antibody-independent isolation of circulating tumor cells by continuous-flow dielectrophoresis](#)

*Biomicrofluidics* **7**, 011807 (2013); 10.1063/1.4774304

[Characterization and separation of \*Cryptosporidium\* and \*Giardia\* cells using on-chip dielectrophoresis](#)

*Biomicrofluidics* **6**, 012805 (2012); 10.1063/1.3671065

[A cell electrofusion microfluidic device integrated with 3D thin-film microelectrode arrays](#)

*Biomicrofluidics* **5**, 034121 (2011); 10.1063/1.3630125

[Numerical modeling of motion trajectory and deformation behavior of a cell in a nonuniform electric field](#)

*Biomicrofluidics* **5**, 021101 (2011); 10.1063/1.3574449

---



**AIP** | Journal of  
Applied Physics

*Journal of Applied Physics* is pleased to  
announce **André Anders** as its new Editor-in-Chief

## Flow-through electroporation of mammalian cells in decoupled flow streams using microcapillaries

Yuan Luo and Levent Yobas<sup>a)</sup>

*Department of Electronic and Computer Engineering, Hong Kong University of Science and Technology, Clear Water Bay, Kowloon, Hong Kong, China*

(Received 26 February 2014; accepted 30 April 2014; published online 21 May 2014)

We report on reversible electroporation of cells in a flow-through microfluidic device, whereby the required electric field is delivered through a set of integrated microcapillaries between a centre stream of cells and side streams of liquid electrolytes. The electrolytes are applied with a sine wave voltage and cells flow by the microcapillary openings encounter a burst of ac field with a duration and strength determined by their average speed and spatial proximity to the microcapillary openings, respectively. Effectiveness of the approach is presented through numerical simulations and empirical results on electroporation efficiency and cell viability against various flow rates (exposure time to the field) as well as frequencies and root-mean-square (rms) intensities of the field. High frequencies (80–400 kHz) and high intensities (e.g., 1.6 kV/cm, rms) are identified with increased electroporation efficiency 61% and viability 86% on average. These results suggest that the device demonstrated here with a simple design and robust operation offers a viable platform for flow-through electroporation. © 2014 AIP Publishing LLC.

[<http://dx.doi.org/10.1063/1.4879155>]

### I. INTRODUCTION

The plasma membrane of cells is an effective barrier and, despite being ~5 nm thin, impermeable to many ions and polar molecules. Yet, in many fields, including drug discovery, gene therapy, antibody production, and regenerative medicine, there has been a growing demand to deliver into cells membrane-impermeable exogenous agents, such as small drugs, proteins, and nucleic acids (e.g., DNA plasmids, siRNA, and mRNA), with minimal or no adverse effects.<sup>1,2</sup> A myriad of intracellular delivery techniques have been adopted using biological<sup>3</sup> (i.e., viral vectors including retroviruses and adenoviruses), chemical<sup>4</sup> (e.g., calcium phosphate, cationic polymers, cationic lipids, and peptides), or physical means<sup>5</sup> (e.g., microinjection, nanoparticle bombardment, optical, sonic, magnetic, and electrical treatment). Viral vectors, although they are known to be the most efficient and effective, carry considerable risks, including acute inflammatory response, cytotoxicity, and oncogenesis.<sup>3</sup> Chemical mediators are variably less efficient and influenced by the properties of mediators and the cell type.<sup>4</sup> In contrast, physical methods, as they directly force cargos into cytosol without any mediator, are relatively safe, more efficient, and particularly effective for transfecting primary, progenitor, and stem cells.<sup>6</sup>

Electroporation, or electropermeabilization, is probably the most popular physical delivery technique as it is simple and works well with many cell types and exogenous targets.<sup>7</sup> Cells are exposed to brief and intense electrical stimuli strong enough to upset their membrane such that tiny pores transiently and reversibly form, through which exogenous cargo can be taken up. The general consensus is that electroporation occurs when the transmembrane potential exceeds the dielectric breakdown voltage of the membrane capacitance (0.2–1.5 V).<sup>8</sup> This requires field strength values in the range of 0.3–2 kV/cm,<sup>9</sup> depending on the cell size. In traditional settings, the field is delivered through high-voltage pulses (>1 kV) by a pair of electrodes embedded in

---

<sup>a)</sup> Author to whom correspondence should be addressed. Electronic mail: eelyobas@ust.hk. Tel.: (+852) 2358–7068.

a cuvette that holds the batch of cells in suspension buffer. The cells are, however, often heterogeneous in size and such one-size-fits-all approach destroys some cells while leaving some others unaffected. For a given cell type, reasonable efficiency and cell viability can only be attained after tedious and extensive trials optimizing electroporation conditions (e.g., electrical pulse width, amplitude, shape, and repetition rate) on the average for the ensemble of cells.<sup>10</sup>

Over a decade ago, Huang and Rubinsky introduced micro-electroporation to tackle these issues and improve efficiency.<sup>11</sup> The method also facilitates further studies on the fundamental physical processes through *in situ* visualization of individual cells during controlled electroporation. Subsequent efforts have mainly focused on the electrode and fluidic designs with advantages and disadvantages as discussed in several recent reviews.<sup>12–15</sup> Briefly, thin-film co-planar electrodes<sup>16</sup> avoid the alignment issue faced in the parallel-plate designs<sup>17</sup> and further reduce the inter-electrode spacing and electroporation voltage. Yet, they expose cells to non-uniform electric fields and suffer from degradation near the edges due to electrolysis. Thick protruded electrodes<sup>18</sup> overcome these issues and establish more of a uniform field, albeit at the expense of fabrication complexity. Alternatively, wire electrodes placed in the reservoirs keep local pH variations and damaging electrolytic bubbles away from the electroporation zone and yet require much higher voltages due to increased inter-electrode spacing.<sup>19</sup> Constrictions introduced along the electroporation zone intensify the local field strength and thus ease the voltage requirement but the method still restricts ionic composition of the medium so as to avoid thermal shock due to joule heating.<sup>20</sup> Many of the systems adopt a continuous-flow electroporation strategy so as to increase throughput. Few of them further harness hydrodynamic principles for increased electroporation effectiveness and better mixing of cells and exogenous cargos.<sup>21,22</sup>

Recently, hydrodynamic flow-focusing technique has been incorporated in micro-electroporation.<sup>23</sup> While the technique continues to rely on wire electrodes placed in reservoirs to avoid the articulated adverse effects, it considerably cuts down the voltage requirement by extending the field through hypertonic sheath flows flanking a focused centre stream of cells. Nevertheless, the configuration is susceptible to disturbances that destabilize liquid-liquid interfaces and the resultant electric field set by the chosen flow rates. The flow-through micro-electroporation system, introduced here, offers enhanced robustness against such disturbances by keeping the centre stream of cells apart from the either hypertonic stream through a thin insulating barrier with an integrated microcapillary array (Fig. 1). The microcapillaries have been previously shown to electroporate cells locally immobilized at their openings.<sup>24,25</sup> Rather than immobilizing cells, the microcapillaries are utilized here such that an effective electrical coupling is established between the stream of cells and the hypertonic streams while maintaining an adequate fluidic decoupling. Moreover, the microcapillaries are attractive alternative to gel-based salt bridges recently introduced into flow through micro-electroporation, as the gels are challenging to integrate and tend to swell by absorbing water over time.<sup>26</sup> We demonstrate the effectiveness of such microcapillaries by electroporating human colon carcinoma cells, under oscillating fields (sine wave), with high efficiency (61%) and viability (86%).

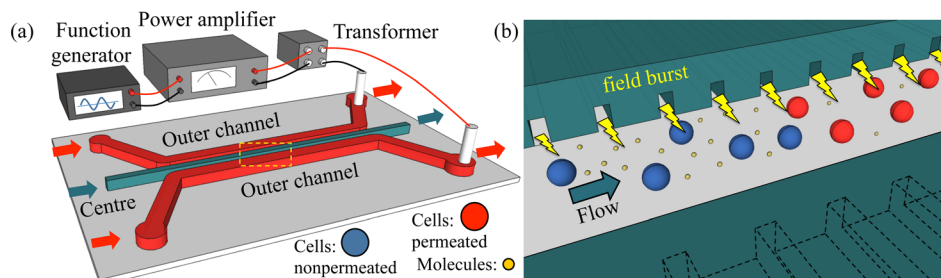


FIG. 1. Conceptual rendering of the flow-through micro-electroporation system based on decoupled flow streams using microcapillaries for electrical coupling. (a) Overall view describing the electrical and fluidic interfacing. The arrows indicate the flow directions. The dashed rectangle outlines the electroporation zone (b), where a centre stream of cells receives a burst of ac field applied to the outer channels and coupled through the microcapillaries.

## II. THEORY

For a spherical cell of radius  $a$  and no surface charge, the position-dependent transmembrane potential,  $\Delta\psi_m$ , induced by an ac oscillating field at a specific point across the cell membrane is described by Schwan's equation,<sup>27</sup>

$$\Delta\psi_m = 1.5aE \cos \theta / [1 + (\omega\tau)^2]^{1/2}, \quad (1)$$

where  $E = E_0 \sin(2\pi ft)$  is the electric field applied, with  $E_0$  and  $f$  being the field intensity and frequency, respectively, and  $t$  being time,  $\omega = 2\pi f$  is the field angular frequency,  $\theta$  is the polar angle between the membrane surface normal and the local field lines, and  $\tau$  is the membrane relaxation time:

$$\tau = aC_m(\rho_i + \rho_e/2), \quad (2)$$

where  $C_m$  is the membrane capacitance per unit area, whereas  $\rho_i$  and  $\rho_e$  represent the intra- and extra-cellular resistivity values, respectively.

From (1), the maximal transmembrane potential occurs at the two loci facing the cathode and anode where  $\theta = 0^\circ$  or  $\theta = 180^\circ$ , respectively. Since  $|\cos \theta| = 1$ , the absolute potential becomes

$$|\Delta\psi_m| = 1.5aE / [1 + (\omega\tau)^2]^{1/2}. \quad (3)$$

According to Eq. (3), the induced transmembrane potential depends on the frequency of the applied field ( $f$ ) and this dependence is stronger around the membrane relaxation time ( $\tau$ ). For a frequency increase from upper kHz range to lower MHz range at constant field strength, cells under physiological conditions experience a sudden drop in their induced transmembrane potential.

## III. MATERIALS AND METHODS

### A. Cells and reagents

HCT116 cells (human colorectal carcinoma cells, ATCC) were cultured in McCoy's 5a (modified) medium supplemented with 10% fetal bovine serum (FBS) in a 37 °C incubator with 5% CO<sub>2</sub> environment. Before each experiment, the cells were detached from the culture dish using trypsin-EDTA treatment and then suspended in the original culture medium. For live staining, the cell suspension was mixed with Calcein-AM (Life Technologies, Inc., NY) at 2 μg/mL and then incubated for absorption at 37 °C for 20 min. Afterwards, the cells were washed twice and resuspended in electroporation buffer (1.5 mM NaCl, 0.03 mM KCl, 0.1 mM Na<sub>2</sub>HPO<sub>4</sub>, 0.02 mM KH<sub>2</sub>PO<sub>4</sub>, and 300 mM D-Mannitol at 100 μS/cm). Propidium iodide (PI, Sigma-Aldrich) was added to the cell suspension as an electroporation indicator at 50 μg/mL before experiments. Cell viability was determined after electroporation using trypan blue exclusion, for which 0.4% trypan blue (Sigma-Aldrich) was added to the cell media at a ratio of 1:10 (v/v). Phosphate buffered saline (PBS) at 15 mS/cm was used as the electrolyte solution in the outer microchannels.

### B. Fabrication

All the devices were replicated in polydimethylsiloxane (PDMS) using silicon-based templates through soft lithography process. The templates involved silicon ridge structures 2 μm wide and raised from the substrate via deep reactive ion etching (DRIE) by 2 μm, 10 μm, or 16 μm, depending on the microcapillary design. On the silicon ridges, negative resist (SU-8, Microchem, MA) was patterned at a thickness value of the desired microchannel depth. The microchannels were fabricated at a depth of 40 μm for the designs with microcapillaries 2 and 10 μm deep while for the design with 16-μm-deep microcapillaries, they were made at a depth

of 30  $\mu\text{m}$ . PDMS (Sylgard 184, Dow Corning, MI) was prepared by mixing and degassing the base material and the curing agent (10:1, w/w) and then cured over the templates for 30 min at 120 °C. The cured PDMS slabs were punched with inlet/outlet holes, and permanently bonded over glass slides upon activating their surfaces via oxygen plasma (40 W, 40 s).

### C. Experiment

The two outer microchannels dedicated to the hypertonic streams were filled with PBS (1 $\times$ ), followed by priming the centre microchannel with electroporation buffer for about 5 min. The sample containing the live-stained cells in electroporation buffer with the added PI was introduced into the centre microchannel in parallel with PBS delivered into the outer microchannels through tubings connected to the inlet ports and at controlled rates using syringe pumps (Harvard Apparatus, MA). Meanwhile, a voltage of sine wave with a root-mean-square (rms) intensity ranging from 35 to 141 V-rms and a frequency from 1 to 400 kHz was constantly delivered without a DC offset from a power supply through a pair of wire electrodes (Cu) placed into the outlet ports of the outer microchannels. It should be noted that the electrodes placed in the ports did not impede the flow. The sample eluted from the centre microchannel was collected in tubing and then transferred onto a glass slide for cell assessment and count. Each count screened 600–1200 cells. Of those viable cells upon electroporation, the permeated fraction defined electroporation efficiency, whereas the viable fraction of all the cells revealed viability. The experiments that visualized fluidic interfaces within the devices were performed at various flow rates with the centre stream free of cells and the hypertonic streams stained with fluorescein (10 mM) and applied with a sine wave of 141 V-rms at two distinct frequencies (1 or 80 kHz). The transfection experiment involved reporter genes expressing modified red fluorescence protein plasmids (mRFP-C3), which were diluted in the buffer to 20  $\mu\text{g}/\text{mL}$  before experiment. Upon electroporation, the cells were collected, transferred to fresh medium in a dish, and cultured while being regularly monitored for gene expression under fluorescence microscope (excitation: 560 nm).

### D. Instruments

An epi-fluorescence microscope (FN1; Nikon, Japan) equipped with a halogen and mercury lamp (100 W) and a CCD camera (RT3 Mono; SPOT, MI) was utilized for device analysis and cell count. Each device was applied with an electrical potential of a sine waveform without a DC offset from a high-voltage transformer (Amp-Line Corp., NY) driven by a function generator (CFG250, Tektronix, Inc., OR) through a wideband power amplifier (AL-50HFA, Amp-Line Corp., NY). An oscilloscope (2205GN, Tektronics Inc., OR) was employed to monitor the waveform.

### E. Simulations

Equations (4)–(9) were solved for the 3D device geometries through finite element method (FEM) analyses on COMSOL Multiphysics Software 3.5 (Comsol Inc., MA) with the following boundary conditions. The respective reservoirs of the outer fluid channels were set at either the ground potential or sine wave with the stated magnitude and frequency. The three inlet ports were assumed to be fixed at the stated flow rates, while the outlet ports were at atmospheric pressure. All the ports along with the lower surface of the glass substrate were assigned  $T_0 = 293.15$  K, while the upper surface of the PDMS slab was described as a free convection boundary  $-k\nabla T = h(T - T_0)$ , with the heat transfer coefficient assigned as  $h = 10$  W m<sup>-2</sup> K<sup>-1</sup>.

The potential distribution across the design  $\varphi$  is given by the Laplace equation

$$\nabla \cdot (\sigma^* \nabla \varphi) = 0, \quad (4)$$

where  $\sigma^* = \sigma + j\omega\epsilon_r\epsilon_0$  is the complex conductivity with real  $\sigma$  (in S m<sup>-1</sup>) and imaginary part:  $\epsilon_r$  is the relative permittivity,  $\epsilon_0 = 8.85 \times 10^{-12}$  F m<sup>-1</sup> is the vacuum dielectric constant, and  $j = \sqrt{-1}$ . The real part varies with temperature  $T$  (in K) as in

$$\sigma = \sigma_0[1 + \alpha(T - T_0)], \quad (5)$$

where the subscript 0 refers to the value at room temperature  $T_0 = 293.15$  K and  $\alpha$  is the electric conductivity coefficient (3%). Both  $\sigma_0$  and  $\epsilon_r$  depend on the spatial coordinates (device domains) with the respective values listed in Table I.

The electric and thermal fields both relate to the simulated potential  $\phi$ , respectively, through  $E = -\nabla\phi$  and the heat-balance equation stated for the fluid domains as

$$\rho C_w u \cdot \nabla T - \nabla \cdot (k \nabla T) = \sigma |\nabla \phi|^2 \quad (6)$$

and for the solid domains (PDMS/glass) as

$$-\nabla \cdot (k \nabla T) = \sigma |\nabla \phi|^2, \quad (7)$$

with  $k$  being the thermal conductivity (in  $\text{W m}^{-1} \text{K}^{-1}$ ),  $\rho$  the density (in  $\text{kg m}^{-3}$ ),  $C_w$  the specific heat capacity (in  $\text{J kg}^{-1} \text{K}^{-1}$ ), and  $u$  the flow velocity (in  $\text{m s}^{-1}$ ) which can be derived from Navier-Stokes and the continuity equations, assuming incompressible viscous flow

$$\rho(u \cdot \nabla)u = \nabla \cdot [-p\mathbf{I} + \eta\{\nabla u + (\nabla u)^T\}], \quad (8)$$

$$\nabla \cdot u = 0, \quad (9)$$

where  $p$  is pressure (in Pa),  $\eta$  is the dynamic viscosity (in Pa s), and  $\mathbf{I}$  is a  $3 \times 3$  identity matrix. The values are given in Table II.

## IV. RESULTS AND DISCUSSIONS

### A. Fluidic design

In each design, a straight microchannel ( $50 \mu\text{m}$  wide) is separated from the two outer parallel-running microchannels ( $30 \mu\text{m}$  wide) via dielectric partitions ( $20 \mu\text{m}$  wide) as described in Fig. 1 (further details in Fig. S1 of the supplementary material).<sup>28</sup> Either partition accommodates an array of microcapillaries, total 13 and evenly spaced apart by  $30 \mu\text{m}$ , interconnecting the microchannels. The microcapillaries are all identical with nominal dimensions  $20 \mu\text{m}$  long,  $2 \mu\text{m}$  wide and, depending on the device, at various depths ( $2$ ,  $10$ , or  $16 \mu\text{m}$ ). All the microchannels are  $40 \mu\text{m}$  deep except those with the  $16\text{-}\mu\text{m}$ -deep microcapillaries, which are kept at  $30 \mu\text{m}$  for a more effective electroporation region.

### B. Electrical coupling

Effectiveness of electrical coupling through the microcapillaries has been evaluated through 3D FEM analyses. Fig. 2(a) shows the electric field distribution across the horizontal midplane on the design with  $16\text{-}\mu\text{m}$ -deep microcapillaries. For an applied potential of  $141$  V-rms at  $80$  kHz, the field strength along the axis of symmetry remains slightly above  $1$  kV/cm, rms. This value is within the electroporation range ( $0.3\text{--}2$  kV/cm).<sup>9</sup> However, the field nearby the microcapillary openings exceeds this range. Fig. 2(a) also shows the electric field profile (lower left) perpendicular to the flow direction across the same design. For comparison, the designs

TABLE I. List of values used for the electric-field analyses.

Domain	$\sigma_0$ ( $\text{S m}^{-1}$ )	$\epsilon_r$
Cell stream	0.01	80
Side streams	1.50	80
PDMS	$0.83 \times 10^{-12}$	2.6
Glass	$1.00 \times 10^{-13}$	4.7

TABLE II. List of values assigned for the thermal-field analyses.

Domain	$\rho$ (kg m <sup>-3</sup> )	$C$ (J kg <sup>-1</sup> K <sup>-1</sup> )	$k$ (W m <sup>-1</sup> K <sup>-1</sup> )	$\eta$ (Pa s)
Streams	$1.00 \times 10^3$	$4.20 \times 10^3$	0.56	0.001
PDMS	$1.03 \times 10^3$	$1.10 \times 10^3$	0.18	...
Glass	$2.23 \times 10^3$	$0.84 \times 10^3$	1.40	...

with 10- and 2- $\mu\text{m}$ -deep microcapillaries are presented as well. The regions with the field intensities outside the electroporation range mount from 30% to 42% of the total volume near 16- and 10- $\mu\text{m}$ -deep microcapillaries. These regions, however, concern only a small fraction of cells, as they are confined to the corners and likely to remain cell free during sample flow due to wall effects. In fact, such a cell-free layer is comparable to the size of a single cell<sup>29</sup> and, given that the average cell diameter here is approximately 12  $\mu\text{m}$ , it is safe to consider that the periphery within 6  $\mu\text{m}$  off the walls is a cell-free layer. Excluding this layer, the rms field intensity averages about 1.6 kV/cm and shows a spatial variation of  $\pm 12\%$  across the channel segment with 16- $\mu\text{m}$ -deep microcapillaries. The segment with 10- $\mu\text{m}$ -deep microcapillaries, although it exhibits a slightly larger variation  $\pm 30\%$ , still remains within the electroporation range around an average value of 0.9 kV/cm. This is not the case for the channel with 2- $\mu\text{m}$ -deep microcapillaries in which cells are unlikely to be altered by the limited effective space near the microcapillary openings. Fig. 2(b) further compares the field strengths across the horizontal midplane of each design along the dashed line in Fig. 2(a). The dashed line bisects the upper half of the channel segment and marks the coordinates along which the rms field intensity values are averaged and used as a representative field intensity for a particular set voltage in the remaining part of the work. It should be noted that these intensity values refer to a time-varying electric field that continuously oscillates. These results suggest that an effective flow-through electroporation of cells in a typical microchannel ( $\sim 50 \mu\text{m}$  wide and deep) requires such microcapillaries at a depth of 10  $\mu\text{m}$  or above.

### C. Fluidic decoupling

It is important that 10- and 16- $\mu\text{m}$ -deep microcapillaries, while offering an effective electrical coupling, be able to keep the adjacent flows decoupled. This has been investigated through experiments where the electroporation buffer and the fluorescent-stained hypertonic solutions

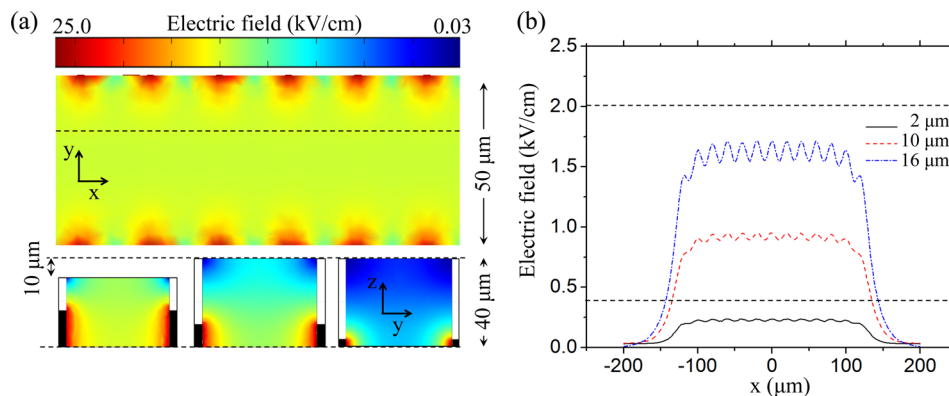


FIG. 2. Simulated electric field coupled through the microcapillaries. (a) Electric field distribution in the centre channel across the horizontal midplane and the plane perpendicular to the flow direction across the device centre (lower panel). The map in the upper panel refers to the design with 16- $\mu\text{m}$ -deep microcapillaries and those in the lower panel reveal all the three designs (note that the color scale is logarithmic). The solid bars on the sides of each map (lower panel) mark the microcapillary depth with respect to the channel. The dashed line (upper panel) delineates the coordinates along which the rms field intensities are given in the subsequent line plots (b) specific to each design with a fixed microcapillary depth (the legend). Horizontal dashed lines in the plot highlight the region of interest for successful electroporation. Boundary condition: 141 V-rms, 80 kHz.

were co-injected into their respective channels at fixed flow rates. A potential difference of 141 V-rms at two distinct frequencies (1 and 80 kHz) was also applied to the hypertonic streams to emulate the conditions in electroporation. Fluorescent micrographs obtained from the design with 16- $\mu\text{m}$ -deep microcapillaries are presented in Fig. S2 of the supplementary material.<sup>28</sup> Since the fluidic resistance of the centre channel is higher than those of the outer channels, identical flow rates (2.7  $\mu\text{L}/\text{min}$ ) lead to the cell stream bleed into the hypertonic streams. A comparable level of leakage is observed in the reverse direction upon nearly a 4-fold increase in the rate of the outer streams to 10.8  $\mu\text{L}/\text{min}$ . Fluidic decoupling becomes favorable with the outer and the centre streams at 5.4 and 2.7  $\mu\text{L}/\text{min}$ , respectively. This state of decoupling is preserved against the deliberate variations in the outer flow rates over a broad range ( $\pm 35\%$ ) regardless of the applied voltage frequency. This suggests that 16- $\mu\text{m}$ -deep microcapillaries offer a certain degree of robustness against flow fluctuations, rendering strict flow control redundant. A slightly wider range is obtained with 10- $\mu\text{m}$ -deep microcapillaries while the streams remain decoupled with the flow rates all delivered at 2.7  $\mu\text{L}/\text{min}$ . No leakage is encountered with 2- $\mu\text{m}$ -deep microcapillaries irrespective of the ratio of the flow rates tested over the range of 1:4 to 4:1. Such decoupling is crucial for keeping the cytotoxic ions and electrolytic bubbles away from the centre stream and also for establishing well-defined electrical boundaries. In the remaining, the ratio of the flow rates between the centre and hypertonic streams is kept at 1:2. In conjunction with flow decoupling, a numerical analysis of thermal loading characteristics of the design is also presented in the supplementary material (Fig. S3).<sup>28</sup>

#### D. Electroporation efficiency and cell viability

Fig. 3 shows a representative group of cells treated in the device with 16- $\mu\text{m}$ -deep microcapillaries and then sequentially imaged for the presence of Calcein-AM, PI, and trypan blue following an incubation period of half an hour. Calcein-AM and PI were applied to the cell suspension before the device treatment. Calcein-AM selectively stains the viable cells as it is membrane permeable and becomes fluorescent upon interacting with active esterases exclusive to the viable cells. PI is membrane impermeable and stains the cells either permanently damaged or reversibly electroporated. It is important to note that trypan blue was administered on the cells after an incubation period subsequent to the treatment and hence could not stain electroporated cells since their membrane had already recovered. Thus, trypan blue assay by exclusively labeling the damaged cells helped us decisively confirm those reversibly porated based on their PI intake and lack of trypan blue. In the images shown, most cells were identified positive for Calcein-AM as well as PI but negative for trypan blue, suggesting that they were mostly viable and electroporated (as those within the rectangles). Few were confirmed permanently damaged: negative for Calcein-AM and positive for PI as well as trypan blue (as those by the arrows). The cells shown were exposed to continuous-flow electroporation with the flow rates kept at 2.7 and 5.4  $\mu\text{L}/\text{min}$ , respectively, for the centre and hypertonic streams while a field intensity of 1.2 kV/cm rms was delivered at 200 kHz.

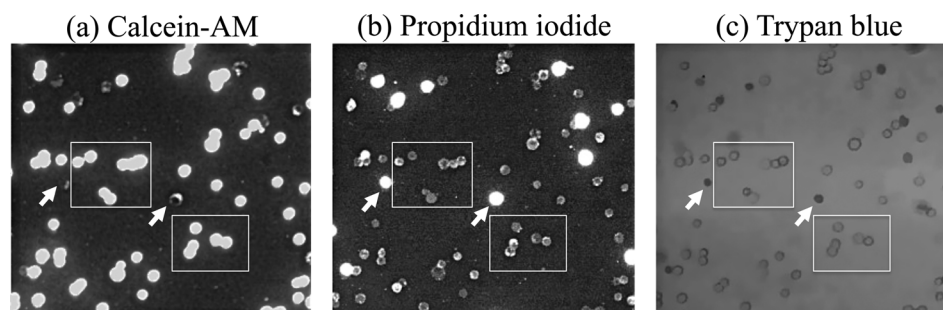


FIG. 3. Fluorescent/bright-field images of the cells following incubation after a continuous-flow electroporation treatment through the design with 16- $\mu\text{m}$ -deep microcapillaries. The images indicate the state of cells for (a) Calcein-AM, (b) PI, and (c) trypan blue staining. The cell stream: 2.7  $\mu\text{L}/\text{min}$ . The field: 1.2 kV/cm rms at 200 kHz.

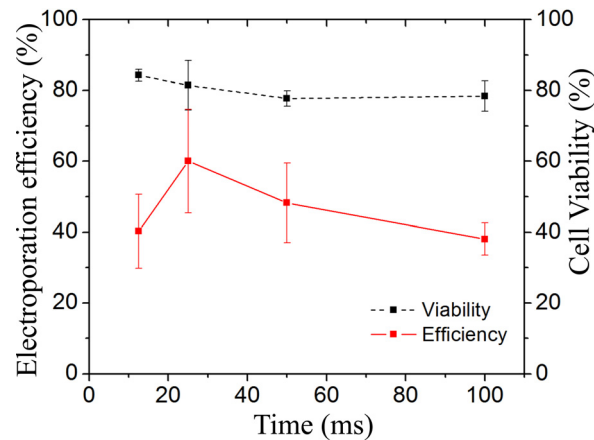


FIG. 4. Electroporation efficiency and cell viability as a function of the exposure time to the field through 16- $\mu\text{m}$ -deep microcapillaries. The exposure time is controlled by the flow rate of the cell stream. The field: 1.6 kV/cm rms at 80 kHz ( $n = 4$ ).

As the applied voltage is a continuous sine wave, cells moving at a constant speed experience a burst of ac field near the microcapillaries. Adjusting the flow rate sets, the time window for which the cells would be exposed to the field. To find the optimal value, electroporation efficiency and cell viability have been evaluated against various flow rates on the same design with the field intensity set at 1.6 kV/cm rms and 80 kHz. The results are presented in a plot as a function of the equivalent burst duration (Fig. 4). Throughout the range, cell viability remains fairly high more or less constant around 80%. Electroporation efficiency makes a peak around 25 ms (corresponding to 2.7  $\mu\text{L}/\text{min}$ ) averaging at 60%. In comparison, Chen *et al.* identified 40 ms optimal for kidney embryonic cells electroporated at 1.4 kV/cm using a train of 5 ms bursts delivered at 20 kHz and with 1 s intervals.<sup>30</sup> It should be noted that, for a higher throughput, the flow rate here could be increased by at least an order of magnitude without causing excessive shear to cells.<sup>31</sup> To maintain the burst duration at 25 ms, however, the electroporation region would be accordingly extended to  $\sim 5$  mm while having microcapillaries appropriately placed along the partitions at equal intervals, which is still manageable within the same device footprint.

Keeping an activation voltage of 141 V-rms at 80 kHz and the centre flow rate at 2.7  $\mu\text{L}/\text{min}$ , the three designs with their distinct microcapillaries have been evaluated and compared in Fig. 5(a). Concurring with our simulations, electroporation efficiency with 2- $\mu\text{m}$ -deep microcapillaries remains poor, averaging at 24% far less than those with 10- and 16- $\mu\text{m}$ -deep microcapillaries. This is because the field coupled through 2- $\mu\text{m}$ -deep microcapillaries remains limited to an intensity of 0.3 kV/cm rms, while reaching 0.9 and 1.6 kV/cm rms through 10- and 16- $\mu\text{m}$ -deep microcapillaries, respectively. Accordingly, with 10- $\mu\text{m}$ -deep microcapillaries, cell viability remains high  $\sim 90\%$  but the average electroporation efficiency falls behind of 16- $\mu\text{m}$ -deep microcapillaries, which is shown to be 60% and with a corresponding viability 80%. The latter two

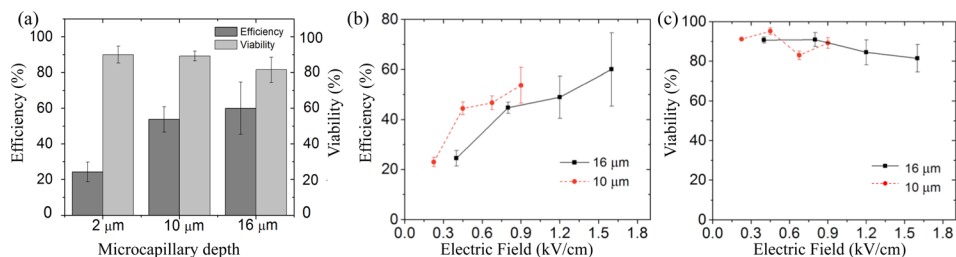


FIG. 5. Dependence of electroporation efficiency and cell viability (a) on the microcapillary depths for a fixed activation voltage (141 V-rms, 80 kHz) and (b) and (c) on the rms field intensities delivered at 80 kHz through the microcapillaries with the indicated depths (legends). The cell stream: 2.7  $\mu\text{L}/\text{min}$  ( $n = 4$ ).

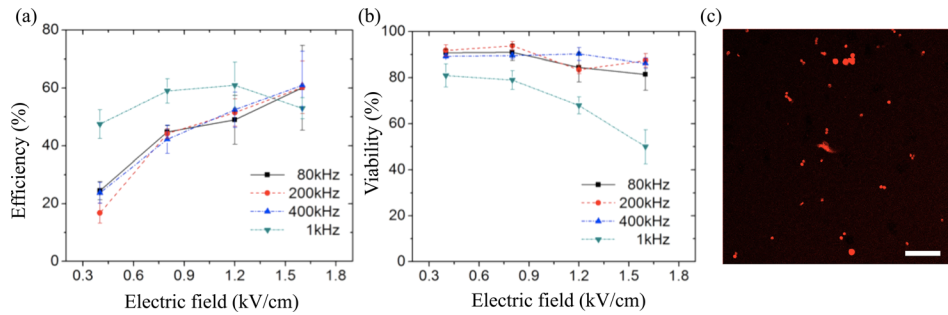


FIG. 6. (a) Electroporation efficiency and (b) cell viability as a function of the rms field intensity delivered at various frequencies (legends) through the design with 16- $\mu\text{m}$ -deep microcapillaries ( $n = 4$ ). (c) Fluorescence image of HCT116 cells successfully transfected with mRFP shown 48 h after electroporation through the same design after being exposed to a field intensity of 1.2 kV/cm rms at 80 kHz. The cell stream: 2.7  $\mu\text{L}/\text{min}$ . Scale bar: 100  $\mu\text{m}$ .

designs have been further compared at reduced field intensities and found comparable as plotted in Figs. 5(b) and 5(c) except that it takes a higher activation voltage to couple similar field strength through 10- $\mu\text{m}$ -deep microcapillaries.

Using the design with 16- $\mu\text{m}$ -deep microcapillaries, the influence of the field frequency on the electroporation process has been investigated for various rms field intensities (Fig. 6). Throughout the range, no notable difference does appear among electroporation efficiencies and viabilities at high frequencies (80, 200, and 400 kHz). Nevertheless, they noticeably deviate from those obtained at a low frequency (1 kHz). Such a weak dependence of the electroporation yield on high-frequency ac fields has also been cited in earlier studies. Chen *et al.* noted no substantial variation in electroporation efficiency over the range of 20–160 kHz.<sup>30</sup> Marszalek *et al.* observed no significant difference in the critical transmembrane potential for electroporation at 0.1–300 kHz.<sup>32</sup> Here, 1 kHz field returns statistically higher efficiencies (mostly above 50%) at lower intensities ( $<1.2\text{ kV}/\text{cm}$ , rms). At higher intensities, however, average efficiency tends to decline falling behind those with high frequency fields. Meanwhile, average cell viability rapidly declines with the increased intensity at 1 kHz. Thus, it is recommended that low frequency fields (in the order of kHz or less) be delivered at lower intensities to minimize cell kill, while high frequency fields (tens of kHz or more) be applied at relatively high intensities to maximize permeable cells. Using the same design and flow conditions, gene transfection and expression for RFP plasmids have also been demonstrated on HCT116 cells treated with a field intensity of 1.2 kV/cm rms at 80 kHz. Fig. 6(c) shows a representative group of cells imaged 48 h after the plasmid transfer. The cells fluorescing red are those having successfully transfected by using the device.

## V. CONCLUSIONS

Through numerical simulations and experiments, we have demonstrated the effectiveness of a flow-through microfluidic device based on the integrated microcapillaries. Using an oscillating electric field, we have evaluated key device features as well as flow rates against electroporation efficiency and cell viability. Cells have been recovered with an average viability of 86% upon high-frequency electroporation ( $\geq 80$  kHz) and of which, 61% on average have been found electroporated. Electroporation efficiency has also been shown monotonically increasing with the field intensity (limited by the power supply). These rates are comparable to those reported for the hydrodynamic flow-focusing technique<sup>22</sup> yet the system introduced here, as it keeps the flow streams decoupled, allows electrolyte flow variation of up to  $\pm 35\%$  for the tested conditions, thereby offering a higher degree of robustness and convenience in device operation.

## ACKNOWLEDGMENTS

The authors thank Professor Randy Poon for access to HCT116 cells and plasmids and Mr. Nelson Lee for plasmid preparation. This project was financially supported in part by the Startup Grant from Electronic and Computer Engineering Department, HKUST, the Research Project

Competition Grant by HKUST (Grant No. RPC11EG09), and Direct Allocation Grant (Grant No. DAG09/10.EG09) by Research Grant Council of Hong Kong.

- <sup>1</sup>T. Niidome and L. Huang, *Gene Ther.* **9**, 1647 (2002).
- <sup>2</sup>F. Toneguzzo and A. Keating, *Proc. Natl. Acad. Sci. U.S.A.* **83**, 3496 (1986).
- <sup>3</sup>C. E. Thomas, A. Ehrhardt, and M. A. Kay, *Nat. Rev. Genet.* **4**, 346 (2003).
- <sup>4</sup>D. W. Pack, A. S. Hoffman, S. Pun, and P. S. Stayton, *Nat. Rev. Drug Discovery* **4**, 581 (2005).
- <sup>5</sup>I. Hapala, *Crit. Rev. Biotechnol.* **17**, 105 (1997).
- <sup>6</sup>A. J. Mellott, M. L. Forrest, and M. S. Detamore, *Ann. Biomed. Eng.* **41**, 446 (2013).
- <sup>7</sup>E. Neumann, M. Schaefer-Ridder, Y. Wang, and P. H. Hofschneider, *EMBO J.* **1**, 841 (1982).
- <sup>8</sup>J. Teissie and M. P. Rols, *Biophys. J.* **65**, 409 (1993).
- <sup>9</sup>E. Tekle, R. D. Astumian, and P. B. Chock, *Proc. Natl. Acad. Sci. U.S.A.* **88**, 4230 (1991).
- <sup>10</sup>D. C. Chang, B. M. Chassy, J. A. Saunders, and A. E. Sowers, *Guide to Electroporation and Electrofusion* (Academic Press, Inc., San Diego, CA, 1992).
- <sup>11</sup>Y. Huang and B. Rubinsky, *Biomed. Microdevices* **2**, 145 (1999).
- <sup>12</sup>S. Wang and L. J. Lee, *Biomicrofluidics* **7**, 011301 (2013).
- <sup>13</sup>M. B. Fox, D. C. Esveld, A. Valero, R. Lutge, H. C. Mastwijk, P. V. Bartels, A. Van Den Berg, and R. M. Boom, *Anal. Bioanal. Chem.* **385**, 474 (2006).
- <sup>14</sup>W. G. Lee, U. Demirci, and A. Khademhosseini, *Integr. Biol.* **1**, 242 (2009).
- <sup>15</sup>S. Movahed and D. Li, *Microfluid. Nanofluid.* **10**, 703 (2011).
- <sup>16</sup>H. Huang, Z. Wei, Y. Huang, D. Zhao, L. Zheng, T. Cai, M. Wu, W. Wang, X. Ding, and Z. Zhou, *Lab Chip* **11**, 163 (2011).
- <sup>17</sup>Y. C. Lin, C. M. Jen, M. Y. Huang, C. Y. Wu, and X. Z. Lin, *Sens. Actuators, B* **79**, 137 (2001).
- <sup>18</sup>H. Lu, M. A. Schmidt, and K. F. Jensen, *Lab Chip* **5**, 23 (2005).
- <sup>19</sup>Y. S. Shin, K. Cho, J. K. Kim, S. H. Lim, C. H. Park, K. B. Lee, Y. Park, C. Chung, D. C. Han, and J. K. Chang, *Anal. Chem.* **76**, 7045 (2004).
- <sup>20</sup>T. Geng, Y. Zhan, H. Y. Wang, S. R. Witting, K. G. Cornetta, and C. Lu, *J. Controlled Release* **144**, 91 (2010).
- <sup>21</sup>J. Wang, Y. Zhan, V. M. Ugaz, and C. Lu, *Lab Chip* **10**, 2057 (2010).
- <sup>22</sup>H. Yun and S. C. Hur, *Lab Chip* **13**, 2764 (2013).
- <sup>23</sup>T. Zhu, C. Luo, J. Huang, C. Xiong, Q. Ouyang, and J. Fang, *Biomed. Microdevices* **12**, 35 (2010).
- <sup>24</sup>M. Khine, A. Lau, C. Ionescu-Zanetti, J. Seo, and L. P. Lee, *Lab Chip* **5**, 38 (2005).
- <sup>25</sup>J. Olofsson, K. Nolkranz, F. Ryttsén, B. A. Lambie, S. G. Weber, and O. Orwar, *Curr. Opin. Biotechnol.* **14**, 29 (2003).
- <sup>26</sup>S. K. Kim, J. H. Kim, K. P. Kim, and T. D. Chung, *Anal. Chem.* **79**, 7761 (2007).
- <sup>27</sup>H. P. Schwan, in *Biological Effects and Dosimetry of Nonionizing Radiation*, edited by M. Grandolfo, S. M. Michaelson, and A. Rindi (Plenum Press, New York, 1983).
- <sup>28</sup>See supplementary material at <http://dx.doi.org/10.1063/1.4879155> for a detailed design schematic and further analyses on fluidic decoupling and thermal loading characteristics.
- <sup>29</sup>M. Faivre, M. Abkarian, K. Bickraj, and H. A. Stone, *Biorheology* **43**, 147 (2006).
- <sup>30</sup>C. Chen, J. A. Evans, M. P. Robinson, S. W. Smye, and P. O'Toole, *Phys. Med. Biol.* **53**, 4747 (2008).
- <sup>31</sup>J. M. Barnes, J. T. Nauseef, and M. D. Henry, *PLoS one* **7**, e50973 (2012).
- <sup>32</sup>P. Marszalek, D. S. Liu, and T. Y. Tsong, *Biophys. J.* **58**, 1053 (1990).